



Journal Name

ARTICLE

A Novel Fabrication Strategy of Doped Hierarchical Porous Biomass-Derived Carbon with High Microporosity for Ultrahigh-Capacitance Supercapacitor

Received 00th January 20xx,
Accepted 00th January 20xx

DOI: 10.1039/x0xx00000x

www.rsc.org/Chengshuai Chang,^{a,c} Miao Li,^{a,c} He Wang,^a Shulan Wang,^{*a} Xuan Liu,^{*a} Huakun Liu^{*b}, Li Li^{*c}

Biomass derived carbons with high surface area, an appropriate pore size distribution, and abundant heteroatoms are viewed as intriguing electrode materials for the assembly of high performance supercapacitors, while how to achieve both the pore structure and the heteroatom engineering simultaneously still remains a challenge. In the present work, we propose a facile and novel synthesis strategy with urea as a micromolecular dual-functional template to prepare an interconnected nitrogen-doped hierarchical porous carbon with high microporosity (86.8%) and small mesopore size (2-4 nm), from Firmiana simplex fluff (FSF) as the biomass precursor. After Co²⁺ catalyzed graphitization and molten KOH treatment, the as-prepared carbon also showed a high surface area (2351 m²/g) and low internal resistance for charge transfer. The as-prepared carbonaceous electrode delivered a record high capacitance value of 836 F/g at a current density of 0.2 A/g in 2 M H₂SO₄. An assembled symmetric supercapacitor also achieved a record aqueous energy density for biochar of 36.50 Wh/kg at the power density of 140 W/kg in 2 M Li₂SO₄. This method provides new insight into the pore structure and defect engineering of carbon and also represents an effective approach to the fabrication of high-capacitance/energy density biochar electrodes.

Introduction

With the advantages of their outstanding reversible charge/discharge rate, high power density, bipolar operational flexibility, and excellent stability, supercapacitors (SCs) have attracted increased interest as next-generation energy storage devices for use in portable devices, smart power sources, and electrical vehicles.¹ Carbon is viewed as one of the most significant candidate electrode materials for high performance SCs due to its advantages of high electrical conductivity, great safety, and large surface area.² Compared with different precursors for preparing carbonaceous materials, such as conductive polymers³ and metal-organic frameworks,⁴ carbon-based material derived from biomass resources is an attractive choice because of its low processing cost, and abundant and renewable material sources, as well as its high potential for industrial large-scale production.⁵ Ideal carbonaceous electrode materials should have a large specific surface area (SSA), appropriate hierarchical porosity integrated with micro-, meso-, and macro-pores, abundant heteroatoms or surface functional groups, and high conductivity for

achieving the high electrochemical performance.⁶ Rational control of the microstructure and elaborate engineering of the porous structure is still a challenge, however, for biochar materials. High microporosity with electrochemically accessible pores (pore size > 0.7-0.8 nm) is theoretically favorable for increasing the capacitive performance and energy density of electrical double layer capacitors (EDLCs), in which charge is accumulated on the electrode/electrolyte interfaces by adsorption/desorption of electrolyte ions.⁷ The isolated micropores with irregular geometry will lead to the lack of sufficient low-resistance channels, however, for electrolyte ions to charge storage sites on the surfaces of the active materials,⁸ and thus mesopores with high SSA are also required. Furthermore, these novel micro/nano-architectures with long range ordered or three-dimensional hierarchical structures are also preferred for carbonaceous materials to provide mass transportation channels and shorten the ion diffusion distance.⁹ In addition to pore structure engineering, heteroatom doping can tune the wettability of carbonaceous electrode and provide extra pseudocapacitance by serving as a source of faradaic reaction sites. Meanwhile, the electrical conductivity of carbon can be further increased by electron-donor heteroatoms.¹⁰ Currently, how to achieve both pore structure and defect engineering simultaneously is still rarely reported, though efforts have been devoted to working on the individual effects in the same material framework.

Here, we propose a novel and feasible strategy to use urea as a micromolecular dual-functional template along with molten KOH for integrating both pore structure and heteroatom engineering in hierarchical porous biomass-derived carbonaceous electrode for high

^a Department of Chemistry, School of Science, Northeastern University, Shenyang 110819, P. R. China. E-mail: slwang@mail.neu.edu.cn, xuanliucmu@gmail.com

^b University of Wollongong, Innovation Campus, North Wollongong, New South Wales 2500, Australia. E-mail: hua_liu@uow.edu.au

^c School of Metallurgy, Northeastern University, Shenyang 110819, P. R. China. E-mail: lilicmu@alumni.cmu.edu, lilicmu@gmail.com

† Electronic supplementary information (ESI) available. See DOI: 10.1039/x0xx00000x

performance SCs. Urea serves as both the nitrogen doping source for in-situ nitridation of biomass carbon with tunable dopant content and also as a micro/mesopore creating template to 1) increase the percentage of micropores in the total surface area and the pore volume contribution, as well as 2) introducing small mesopores 2–4 nm in size to provide buffer space to minimize the ion diffusion distances to charge storage sites. Instead of using the conventional hard templates that need additional removal processes or soft templates with macromolecules that make it hard to achieve control of the geometry, the use of urea as a simple micromolecular dual-functional template combined with Co^{2+} catalytic graphitization and molten KOH treatment enabled us to successfully achieved the fabrication of in-situ N doped interconnected hierarchical porous carbon from Firmiana simplex fluff (FSF). KOH serving as the activation agent can introduce the pores by chemically etching the carbon with the release of gases while the metal potassium vapor produced can intercalate into carbon for lattice expansion and aromatic layer distortion.¹¹ Meanwhile, the graphitization degree of carbonaceous materials is also damaged by KOH activation. The addition of Co^{2+} can be converted to cobalt oxide and metallic cobalt during carbonization, which can serve as the catalyst and template in transforming the amorphous carbon into graphitized carbon with increased graphitization degree.¹² Co and its compounds are then removed through acid washing before electrochemical characterization.¹² Compared with most reported biomass derived carbonaceous electrodes with specific capacitances smaller than 400 F/g, a record high gravimetric capacitance for biochar was achieved (836 F/g at the current density of 0.2 A/g) for the as-prepared materials, with an ultra-high volumetric capacitance of 426.6 F/cm³ also obtained. Moreover, the high energy density of 36.50 Wh/kg was delivered at the power density of 100 and 140 W/kg in 2 M Li_2SO_4 . To the best of our knowledge, this is also the record value for biomass derived carbon in aqueous electrolyte. This work provides a simple and feasible fabrication strategy for doped carbon materials with both pore structure and heteroatom engineering for supercapacitors, and may be extended to other energy conversion and storage fields to promote materials/methodological innovation.

Experimental

Materials

Cobalt nitrate ($\text{Co}(\text{NO}_3)_2 \cdot 6\text{H}_2\text{O}$) and ammonium chloride (NH_4Cl) were obtained from McLean chemical reagent co. LTD. Urea (CON_2H_4), potassium hydroxide (KOH) and melamine ($\text{C}_3\text{H}_6\text{N}_6$) were supplied by Sinopharm group chemical reagent co. LTD. All reagents are of analytical grade and used as received without further purification.

Sample preparation

FSF was soaked in 15 wt% NaOH solution at 60 °C for 12 h under magnetic stirring and then washed with deionized water until the pH became neutral. 2.2 g of dried FSF was immersed in 200 mL of 0.05 M $\text{Co}(\text{NO}_3)_2$ for 12 h under magnetic stirring for complete Co^{2+} impregnation. The treated FSF was then put into 4.4 g/10 mL KOH solution together with a fixed amount of urea (CON_2H_4) in the mass ratios of 1:1, 1:2, and 1:3 (FSF to CON_2H_4) with stirring continued overnight. The as-prepared mixture was then calcined at 300 °C for 1

h, followed by 700 °C for 1 h with the heating rate of 5 °C/min under N_2 gas flow. The prepared samples were washed with 0.2 M HCl and filtrated with deionized water to remove the by-products introduced by Co^{2+} addition, following by drying at 60 °C for 24 h. The samples were designated according to the mass ratio of FSF to CON_2H_4 as HN-DP-FSFC-1, HN-DP-FSFC-2, and HN-DP-FSFC-3, respectively. The control sample with no added KOH or CON_2H_4 was designated as FSFC, while with KOH added but not CON_2H_4 was designated as HP-FSFC. The freeze-drying technique was applied to some samples to introduce more macropores as a comparison with conventional drying methods while we also want to explore if the electrochemical performance of samples can be improved. NH_4Cl and $\text{C}_3\text{H}_6\text{N}_6$ were also used as different nitrogen sources instead of CON_2H_4 to investigate the doping influence on the microstructure and electrochemical performance of the as-prepared carbon. In addition, samples of the dried FSF were also immersed in 200 mL H_2O , 0.05 M $\text{Co}(\text{NO}_3)_2$, and 0.05 M methyl orange or methylene blue, respectively, for 12 h under magnetic stirring to test the adsorption capability of the raw materials.

Materials Characterization

Transmission electron microscopy (TEM) under different magnifications was performed on a probe aberration-corrected JEOL JEM-2100 at an accelerating voltage of 200 kV with high resolution TEM (HRTEM) images also recorded. Scanning electron microscopy (SEM) and energy dispersive X-ray spectroscopy (EDS) were conducted on a Hitachi S-4800 and INC 250 with the accelerating voltage of 5 kV. Thermogravimetric analysis (TGA) and differential thermal analysis (DTA) of CON_2H_4 were carried out to analyze its thermodynamic behavior on a differential scanning calorimetry/TGA (DSC-TGA) instrument (TA Instruments model SDT 2960) at a heating rate of 5 °C/min in N_2 atmosphere from room temperature to 700 °C. The wetting properties of samples were measured on a contact angle measurement instrument (XG-CAMA1). Raman spectra were obtained with an excitation wavelength of 532 nm at room temperature by laser confocal Raman microspectroscopy. X-ray diffraction (XRD) patterns were collected using $\text{Cu K}\alpha$ radiation ($\lambda = 1.5418 \text{ \AA}$) with a scanning speed of 10°/min between 10° and 70° on a D8 ADVANCE (Bruker AXS). X-ray photoelectron spectroscopy (XPS) was conducted on an ESCALAB 250 spectrometer using a $\text{Cu K}\alpha$ radiation excitation source ($\lambda = 1.54178 \text{ \AA}$). The N_2 adsorption/desorption isotherms were measured using an American Micromeritics ASAP-2020 analyzer at 77.1 K.

Electrochemical Measurements

Cyclic voltammetry (CV), galvanostatic charge/discharge (GCD) measurements, and electrochemical impedance spectroscopy (EIS) were performed on a CHI 660D electrochemical workstation. The as-prepared sample was mixed with acetylene black and polyvinylidene fluoride (PVDF) in a ratio of 80:10:10 in a moderate amount of *N*-methyl-2-pyrrolidone (NMP) and then was coated on stainless steel mesh ($1 \times 1 \text{ cm}^2$ in area) with the mass loading of the sample controlled to be approximately 2.0 mg as the working electrode. Platinum foil and saturated calomel electrode were selected as the counter and reference electrodes. CV, GCD, and EIS curves were measured in different electrolytes, including 2 M H_2SO_4 , 2 M Li_2SO_4 (pH=1.8), 2 M KOH, 1 M Na_2SO_4 , and 2 M MgSO_4 ,

respectively. EIS was conducted in the frequency range of 0.01 to 10^5 Hz at open circuit voltage under ac amplitude of 5 mV. The gravimetric capacitance (C_g , F/g) was evaluated according to the GCD curves based on the following equation:

$$C_g = I \times \Delta t / (m \times \Delta V) \quad (1)$$

where I is the current (A), ΔV the discharge potential window (V), Δt the discharge time (s), and m the loading mass of active material (g).

The volumetric capacitance was calculated according to the following equations:¹¹

$$C_v = C_g \rho \quad (2)$$

$$\rho = 1 / (V_{\text{pore}} + 1/\rho_{\text{carbon}}) \quad (3)$$

where C_v is the volumetric capacitance (F/cm³), C_g the gravimetric capacitance (F/g), ρ the particle density (g/cm³) (the density of monoliths is used), V_{pore} the total pore volume (cm³/g), and ρ_{carbon} the true density of carbon (2 g/cm³).

In the symmetrical SCs, the two working electrodes with the same mass loading (2 mg) of the three-electrode setup were separated by sulfonation membrane and assembled in a sandwich structure with two polytetrafluoroethylene sheets impregnated with electrolytes consisting of 2 M H₂SO₄ and 2 M Li₂SO₄, respectively. Two-electrode symmetrical SCs cells (CR2025-type coin cell) were also assembled using 1 M 1-butyl-3-methylimidazolium tetrafluoroborate/acetonitrile (BMIMBF₄/AN) as electrolyte. The specific capacitance, energy density, and power density of the symmetrical SCs were calculated based on Equations (4)-(6):

$$C_{\text{cell}} = I \times \Delta t / (M \times \Delta V) \quad (4)$$

$$E_{\text{cell}} = C_{\text{cell}} \times \Delta V^2 / (2 \times 3.6) \quad (5)$$

$$P_{\text{cell}} = 3600 \times E_{\text{cell}} / \Delta t \quad (6)$$

Where E_{cell} is the energy density (Wh/kg), P_{cell} the power density (W/kg), C_{cell} the specific capacitance (F/g), ΔV the cell voltage (V) for charging and discharging, and Δt the discharge time (s), respectively.

Results and discussion

The detailed synthetic flow of the CON₂H₄-assisted templated fabrication of N-doped hierarchical porous carbon is shown in Fig. 1A, with optical images of the product in each step presented in Fig. S1 in the Supporting Information. Herein, the reasons that inspired us to selecting FSF as the biomass precursor are: 1) It is abundant in nature, while the lack of an efficient recycling method leads to a huge waste of resources. 2) More importantly, the special inherent tubular structure of FSF (Fig. S2) endows the precursor with strong adsorption capability for organic dyes and salt solution (Fig. S3), indicating that Co²⁺ ions as well as KOH, CON₂H₄, and water molecules can easily penetrate into the cell walls of FSF, which can ensure complete interaction between the metal ions and the biomass precursor for carbonization, as well as a more uniform activation process for pore structure formation.¹¹ In addition, this microtubular structure can be well maintained even after carbonization (radial directional view in Fig. 1B and Fig. S4), which provides efficient natural mass transfer channels for electrolyte ions and electrons to diffuse through the carbon framework with low resistance. This may also provide some clues from the material itself as to why the FSF presented in the current work showed remarkable electrochemical performance compared with other reported biomass sources. Unlike

the conventional KOH mixing for activation during the annealing,¹³ KOH introduced into the cell walls of biomass precursor through the pre-immersive treatment can serve as the framework scaffold to avoid the coalescence of cell walls and enable more pores generated.¹¹ Meanwhile, molten KOH as the carbonization medium has excellent chemical solubility and reactivity for facilitating the breaking of chemical bonds in the biomass precursor during annealing, which is favorable for the formation of a uniform pore structure.⁵ Herein, CON₂H₄ serves as a dual-functional template: namely, the in-situ nitrogen doping source and the template for creating micropores/small mesopores during carbonization. CON₂H₄ (and its decomposed derivative) with micromolecular structure can take up the space after pre-impregnation into the cell walls of FSF to serve as the micropore creating template during carbonization. In addition, the release of CO₂ arising from the decomposition can further activate the carbonaceous materials to introduce micropores and small mesopores, while NH₃ or N based decomposition derivatives can nitride the carbon.

Fig. 1C is a top view of HN-DP-FSFC-2. The walls are composed of honeycomb-like interconnected macropores 300±120 nm in size (Fig. 1C and 1D). Without the addition of CON₂H₄ (HP-FSFC), the morphology and macroporous structure showed no apparent change (Fig. S5) with the formation of a similar honeycomb-like structure, indicating CON₂H₄ activation did not lead to the obvious introduction of macropores. In contrast, it is well known that the freeze-casting technique can introduce macropores,¹⁴ but in this case it can be seen that the introduction of further macropores from freeze casting leads to the collapse of macroporous structure (Fig. S6). HN-DP-FSFC-1 (Fig. S7) and HN-DP-FSFC-3 (Fig. S8) with the different CON₂H₄ dosages also showed similar morphologies and macroporous structure. Note that, when the nitrogen source is changed to NH₄Cl (Fig. S9) or C₃H₆N₆ (Fig. S10), the porous structure is severely damaged, with only carbon fragments and mass agglomerations being formed. The EDS results (Fig. 1E) showed that the hetero-elements N, O, and S are uniformly distributed through the interconnected framework without hot spots for agglomeration being observed. The presence of heteroatoms is crucial for improving the electrochemical performance of carbon, since they can introduce Faradaic pseudocapacitance via additional redox reactions.¹⁵ Bright field TEM (Fig. 1F) and HRTEM (Fig. 1G) images confirmed the presence of mesopores 2-4 nm in size and micropores in HN-DP-FSFC-2. The interlayer spacing of HN-DP-FSFC-2 was measured to be 0.36 nm, which is larger than that of graphite (0.34 nm), indicating the heteroatoms doping enlarged the spacing between different carbon layers.¹

The carbon structure and degree of graphitization were characterized by Raman spectroscopy, and the spectra are shown in Fig. 2A. The peaks at 1339 and 1577 cm⁻¹ refer to the D and G bands, which characterize the defective/disordered carbon and the graphitic phase, respectively.¹⁶ The intensity ratio (I_G/I_D) value decreased from 1.36 for FSFC and 1.28 for HP-FSFC to 1.00 (HN-DP-FSFC-1), 0.95 (HN-DP-FSFC-2), and 0.94 (HN-DP-FSFC-3), indicating that the addition of CON₂H₄ led to decreased graphitization for the as-prepared carbon. Higher CON₂H₄ content leads to a lower value of I_G/I_D and introduces more disordered structure into the porous carbon. More gases can be released through thermal decomposition of CON₂H₄ for carbon activation, and in the meantime, more N

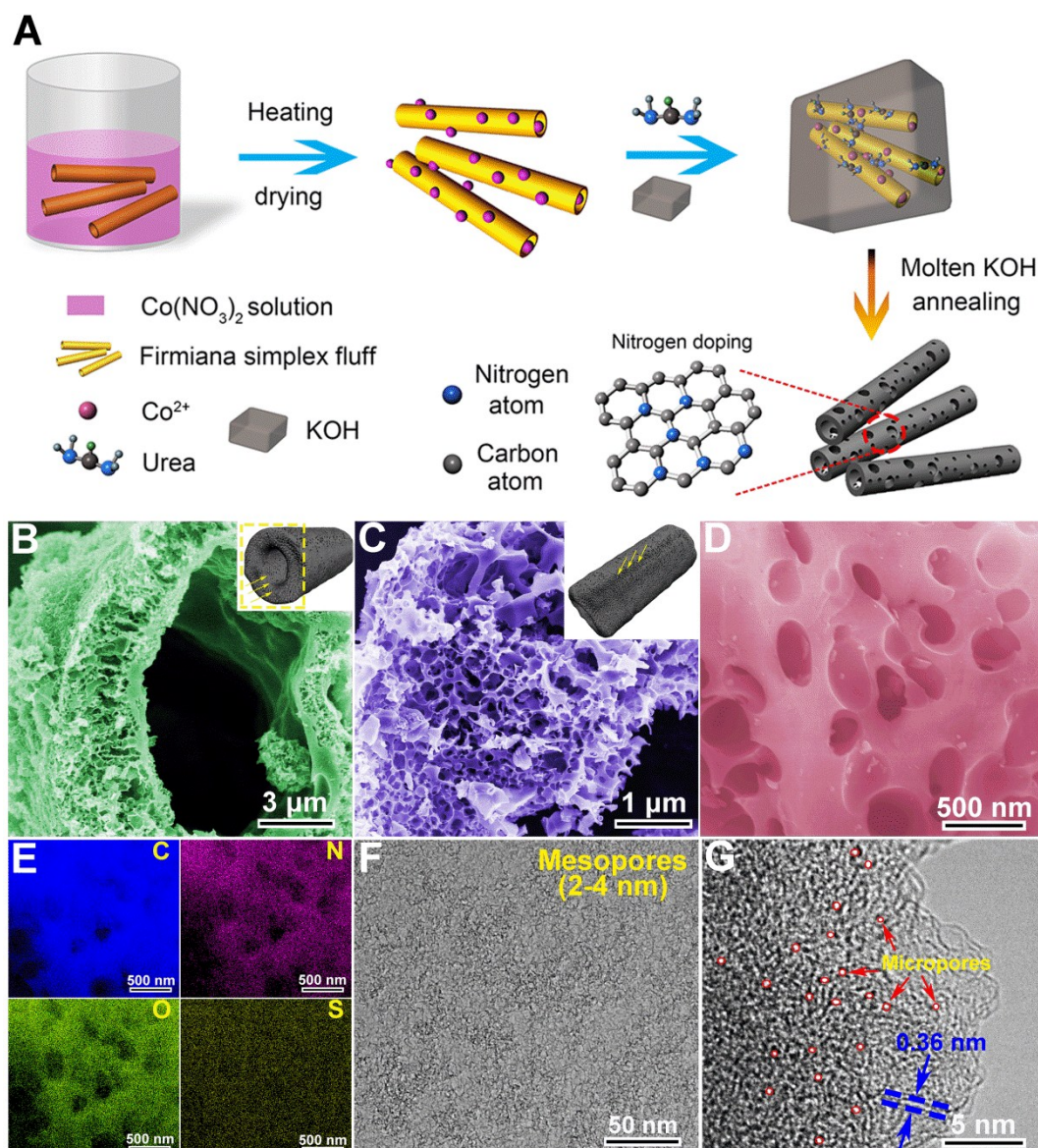


Fig. 1 (A) Schematic illustration of synthetic flow for the CON_2H_4 -assisted template fabrication of N-doped hierarchical porous carbon; SEM images of tubular structure from (B) the horizontal direction, (C) view of the surface from the radial direction, with the insets showing the direction, and (D) high magnification image of the tube wall; (E) corresponding EDS elemental mapping; (F) bright field TEM image and (G) high-resolution image of HN-DP-FSFC-2.

defects are introduced to disorder the carbon layers.¹⁷ This is consistent with the results that the surface area and porosity increased (Table S1) with increasing CON_2H_4 dosage, while N-5 and N-6 contents (Fig. 1H and Table S2) also rose. The XRD patterns of the samples are shown in Figure 2B. The sharp peaks at 25.2° and 44.1° for FSFC, which are related to the (002) and (100) planes of the graphitic-type lattice, indicate that the carbon treated by Co^{2+} can maintain a high degree of graphitization, while Co^{2+} can serve as a template catalyst to promote the formation of graphitic carbon.¹⁸ High graphitization degree which leads to the conductivity improvement and thus facilitation of electron transport during the electrochemical process is preferred. The addition of Co^{2+} can

balance the decrease in graphitization introduced by KOH and CON_2H_4 activation and keep it within a reasonable range.^{12,18} The electrical conductivity values of the samples treated with and without the addition of Co^{2+} are added in Table S3. Consistent with the Raman results shown in Fig. 2A, the (002) and (100) peaks of HP-FSFC and HN-DP-FSFC-2 are broadened with decreased intensities, confirming their reduced graphitization. Meanwhile, the shift of their (002) peaks to lower reflection angle confirms the expansion of their carbon layers, which is consistent with the HRTEM image (Fig. 1G).

To further investigate the role of CON_2H_4 as a dual-functional template for nitrogen doping and activation, TGA/DTA were carried

out on CON_2H_4 to investigate its thermodynamic behavior, as shown in Fig. 2C. The whole curve can be divided into four regions, corresponding to the different decomposition stages of CON_2H_4 . The detailed stepwise decomposition reactions of CON_2H_4 and their corresponding TGA/DTA regions are listed in Table S4. In addition to nitrogen doping, the release of CO_2 can serve as the activation agent for the in-situ etching of the carbonaceous materials and its expansion effect, together with NH_3 and other gases during CON_2H_4 decomposition (Table S4), and it can enlarge some of the pores to 2-4 nm in the mesopore size range.^{9,19} The thus-produced NH_3 and carbon nitride with electron-rich nitrogen species can introduce various N functionalities into graphite network (See Fig. 1G).²⁰

Excellent electrode wettability towards the electrolyte is crucial for achieving high capacitive performance, since more electroactive sites can be accessible to the electrolyte ions.²¹ The presence of hydrophilic heteroatoms, such as N, O, and S, can improve the affinity of carbonaceous materials towards electrolyte.^{9,22} All of the as-prepared samples in the current case are wettable, with the contact angle (θ) value of 41.1°, 36.4°, 31.6°, 26.2°, and 24.3° for FSFC, HP-FSFC, HN-DP-FSFC-1, HN-DP-FSFC-2, and HN-DP-FSFC-3 (Fig. 2D), respectively. The wettability increased (θ smaller) with increasing CON_2H_4 content. The surface area and pore structure were analyzed by Brunauer-Emmett-Teller (BET) measurements (Fig. 2E and Table S1). Compared with FSFC and HP-FSFC with SSA of 325 and 1154 m^2/g , respectively, the samples with addition of CON_2H_4 showed higher values of 1385 (HN-DP-FSFC-1), 2351 (HN-DP-FSFC-2), and 2834 (HN-DP-FSFC-3) m^2/g , indicating the

increased activation of carbon by the gases released from CON_2H_4 . The pore volume also increased from 0.20 and 0.78 cm^3/g for FSFC and HP-FSFC to 0.96, 1.46, and 2.09 cm^3/g for HN-DP-FSFC-1, HN-DP-FSFC-2, and HN-DP-FSFC-3, respectively. Note that the addition of CON_2H_4 leads to more mesopores in the size range of 2-4 nm (as shown in the pore size distributions of the samples in Fig. S11). The presence of small mesopores (2-4 nm) is favorable for increasing the capacitance of carbon because both a Helmholtz layer and buffering diffusion spaces exist on the surfaces of the active material with the smallest distance for ion adsorption.⁹ A larger mesopore size can lead to a longer diffusion distance for the ions and electrons to reach the micropores. Another key feature introduced by the CON_2H_4 addition for carbonaceous materials is the increased percentage of micropores among the total pores. As shown in Fig. 2F and Table S1, the $S_{\text{micro}}/S_{\text{total}}$ and $V_{\text{micro}}/V_{\text{total}}$ values, where V_{micro} (V_{total}) and S_{micro} (S_{total}) are the micropore (total pore) volume and micropore (total pore) surface area, respectively, of the HN-DP-FSFC samples are significantly higher than for FSFC and HP-FSFC, while HN-DP-FSFC-2 shows the highest values ($S_{\text{micro}}/S_{\text{total}} = 86.81\%$, $V_{\text{micro}}/V_{\text{total}} = 76.71\%$) among all the samples. Meanwhile, compared with HP-FSFC, the micropore size of the HN-DP-FSFCs shows an apparent shift to a larger dimension, with the primary size in the range of 0.7-1.7 nm, which is electrochemically accessible for electrolyte ions.^{9,23} In other words, apart from introducing micropores, the addition of CON_2H_4 also assists in the conversion of some “dead” micropores to electrochemically active pores. Rich micropores are one of the most crucial factors needed to achieve

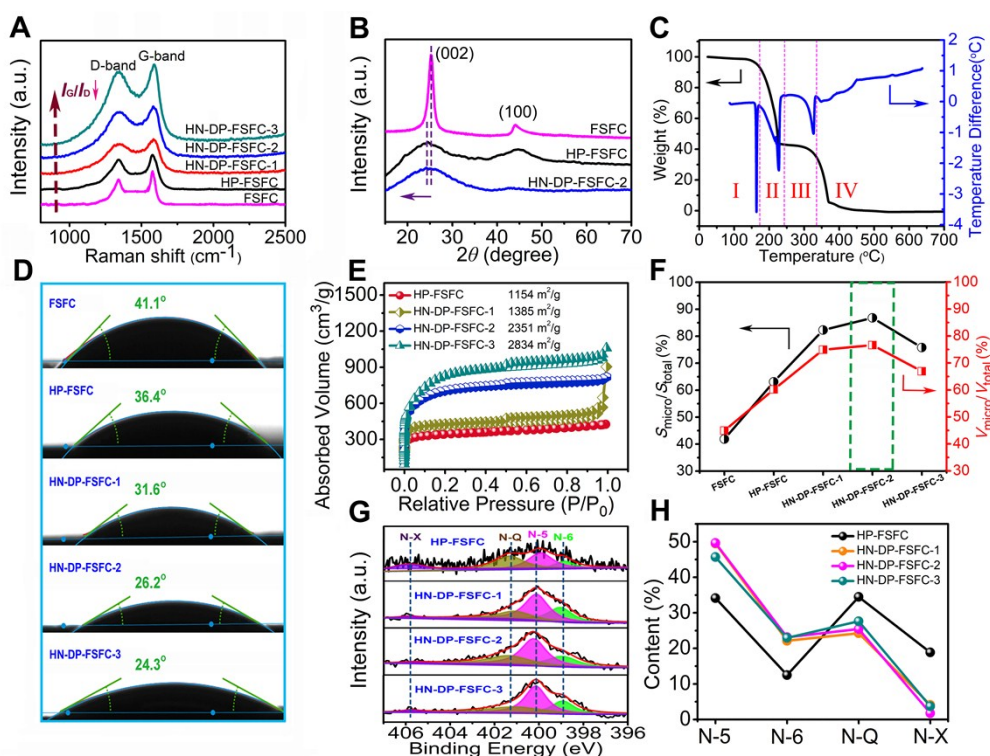


Fig. 2. (A) Raman spectra, and (B) XRD spectra of the as-prepared samples; (C) TGA and DTA curves of CON_2H_4 ; (D) Measurements of contact angle and wettability; (E) N_2 adsorption and desorption isotherms and (F) $S_{\text{micro}}/S_{\text{total}}$ and $V_{\text{micro}}/V_{\text{total}}$ of as-prepared samples; (G) High-resolution N 1s XPS spectra, and (H) content percentages of corresponding N species.

high electrical-double-layer capacitance.²² The high microporosity of the as-prepared materials may originate from the small molecular clusters of CON_2H_4 , which can occupy space in the cell walls of FSF during impregnation and release CO_2 as well as other small-molecule gases from the inner surface of a cell for in situ-activation.

Quantitative information on surface elements and functional groups as well as valence states of the as-prepared samples were obtained by XPS. High resolution N spectra are shown in Fig. 2G and other elements in Fig. S12. Four peaks at 398.8, 400.2, 401.8, and 405.8 eV in the N 1s spectra of all the samples are related to the pyridinic-N (N-6), pyrrolic-N (N-5), quaternary-N (N-Q), and oxidized nitrogen species (N-X), respectively, with the detailed contents shown in Fig. 2H and Table S5. N-5 is the predominant N-containing group for the samples, with values of 34.15, 49.49, 49.65, and 45.69 % for HP-FSFC, HN-DP-FSFC-1, HN-DP-FSFC-2, and HN-DP-FSFC-3 (Table S2), respectively. N-5 and N-6 species are the important contributors for boosting the capacitive performance in supercapacitors by introducing electron donors for conjugation with π -conjugated rings and offering sufficient electrochemically active sites.^{1,24,25} It can be clearly observed from Fig. 2G that the contents of N-5 and N-6 species are significantly increased for HN-DP-FSFC samples compared with HP-FSFC, while HN-DP-FSFC-2 shows the highest values (49.65% and 23.15% for N-5 and N-6, respectively, Table S2) among all the samples.

Four peaks at 284.5, 284.8, 286.1, and 288.9 eV in the high-resolution C 1s spectrum (Fig. S12G) refer to C=C, C-C, C-O/C-N and C=O, respectively. The O 1s spectrum can be deconvoluted into three peaks at the binding energies of 531.5, 532.6, and 533.5 eV which are assigned to C=O, C-O-C, and C-OH, respectively (Fig. S12H). These bonds can introduce extra pseudocapacitance and enhance the wettability of electrodes.²² The high-resolution S 2p spectrum consists of three peaks with binding energy of 164.8, 165.3 and 168.5 eV (Fig. S12I), corresponding to S 2p_{3/2}, S 2p_{1/2}, and oxidized sulfur, respectively.^{26,27} Table S5 shows the element contents of C, O, N and S for all the samples. It should be noted that the N content increased dramatically from 2.12 (FSFC) and 1.63 wt% (HP-FSFC), which originated from the self-heteroatom doping in the biomass precursor, to 2.55 (HN-DP-FSFC-1), 3.43 (HN-DP-FSFC-2), and 5.78 wt% (HN-DP-FSFC-3) with increasing CON_2H_4 content. The use of urea leads to the change of element contents in the samples.

The electrochemical performances of as-prepared samples were evaluated in the three-electrode configuration in 2 M H_2SO_4 aqueous electrolyte within the potential window of -0.15–0.85 V. The results are shown in Fig. 3. The cyclic voltammograms (CVs, Fig. 3A) of FSFC and HP-FSFC without CON_2H_4 nitridation show a regular rectangular shape with a slight deviation (Fig. 3A and Fig. S12) due to the pseudocapacitance of the inherent heteroatoms N, O, and S from the biomass precursor.²⁸ Their EDLC and pseudocapacitive performances are still poor, however, with low CV responses, although KOH activation improved the capacitive performance slightly for HP-FSFC. In contrast, the electrochemical performance of HN-DP-FSFC is significantly enhanced with a higher current response to 10–20 A/g, especially for HN-DP-FSFC-2, indicating the high capacitance and also high energy storage potential of the

samples after the addition of CON_2H_4 . Apart from the double layer capacitance from the approximately rectangular CV curves, the symmetric broad humps of redox peaks for HN-DP-FSFC are related to the Faradaic processes from heteroatoms introduced by nitridation, leading to a pseudocapacitance contribution.¹ Figure 3B shows CV curves of HN-DP-FSFC-2 at different scan rates within the potential range of 5–100 mV/s. The highly expanded current densities with increasing sweep rate demonstrate that both the pseudocapacitive and electrical double layer-like processes have excellent reversibility and rate performance.²³ The CV curves of HN-DP-FSFC-2 exhibited the highest area compared with the other samples (Figs. S13 and S14), indicating its outstanding capacitive performance compared to the other samples. The GCD curves of all the samples at different current densities are shown in Figs. 3C, S13, and S14, while the corresponding capacitances were obtained and are plotted in Fig. 3D. The appearance of nonlinear and bent GCD curves (Figs. S13 and S14) for the HN-DP-FSFCs demonstrates their highly pseudocapacitive behavior arising from heteroatoms. In contrast, the bending of GCD curves for FSFC is lower, indicating the small capacitive contribution from pseudocapacitance. HN-DP-FSFC-2 shows the largest bending along with extremely high capacitance values (Fig. 3D) of 836, 593, 545, 486, 456, 420, 384, 370, 330, and 300 F/g at the current densities of 0.2, 0.5, 1.0, 2.0, 3.0, 5.0, 8.0, 10, 15, and 20 A/g, respectively, which are much better than those of the control samples and other reported reference samples (Fig. 3E). When the loading mass was increased to 5 mg/cm², HN-DP-FSFC-2 still showed a high capacitance values of 728, 532, 463, 429, 395, 364, 328, 311, 287, 260 F/g at the current density of 0.2, 0.5, 1.0, 2.0, 3.0, 5.0, 8.0, 10, 15, 20 A/g respectively. The corresponding CV curves and GCD profiles of the sample were shown in Fig. S15. To the best of our knowledge, these represent the record values for the capacitance of biomass derived carbonaceous materials (Table S6). Correspondingly, this sample also showed ultra-high volumetric capacitance (C_v) of 426.6, 302.4, 278.0, 247.9, 232.6, 214.2, 195.8, 188.7, 168.3, and 153.0 F/cm³ at the current densities of 0.2, 0.5, 1.0, 2.0, 3.0, 5.0, 8.0, 10, 15, and 20 A/g, respectively (Figure 3F), which makes it one of the highest performance biochar materials.^{38–40} Higher or lower CON_2H_4 contents lead to decreased capacitance, while all the HN-DP-FSFC samples showed higher values than HP-FSFC, indicating that the nitridation and activation from CON_2H_4 can improve the capacitive performance of as-prepared carbon. In addition, the control sample HN-DP-FSFC-2, which was treated by freeze-casting to introduce more macropores, showed lower values of 569, 484, 426, 368, 354, 324, 289, 268, 234, and 216 F/g at the current densities of 0.2, 0.5, 1.0, 2.0, 3.0, 5.0, 8.0, 10, 15, and 20 A/g, respectively (Fig. S16). These values indicate that the optimized pore structure is one of the key contributors to high capacitive performance.

The EIS results for the as-prepared samples with Nyquist plots in the range of 0.01 and 10⁵ Hz are shown in Fig. 3G. The high frequency region is magnified and presented in the inset. The Nyquist plots consist of steep linear curves in the low-frequency segment, which is due to near-ideal capacitive behavior, and semicircles in the high-frequency segment with diameters reflecting the charge transfer resistance (R_{ct}) and intercept points on the

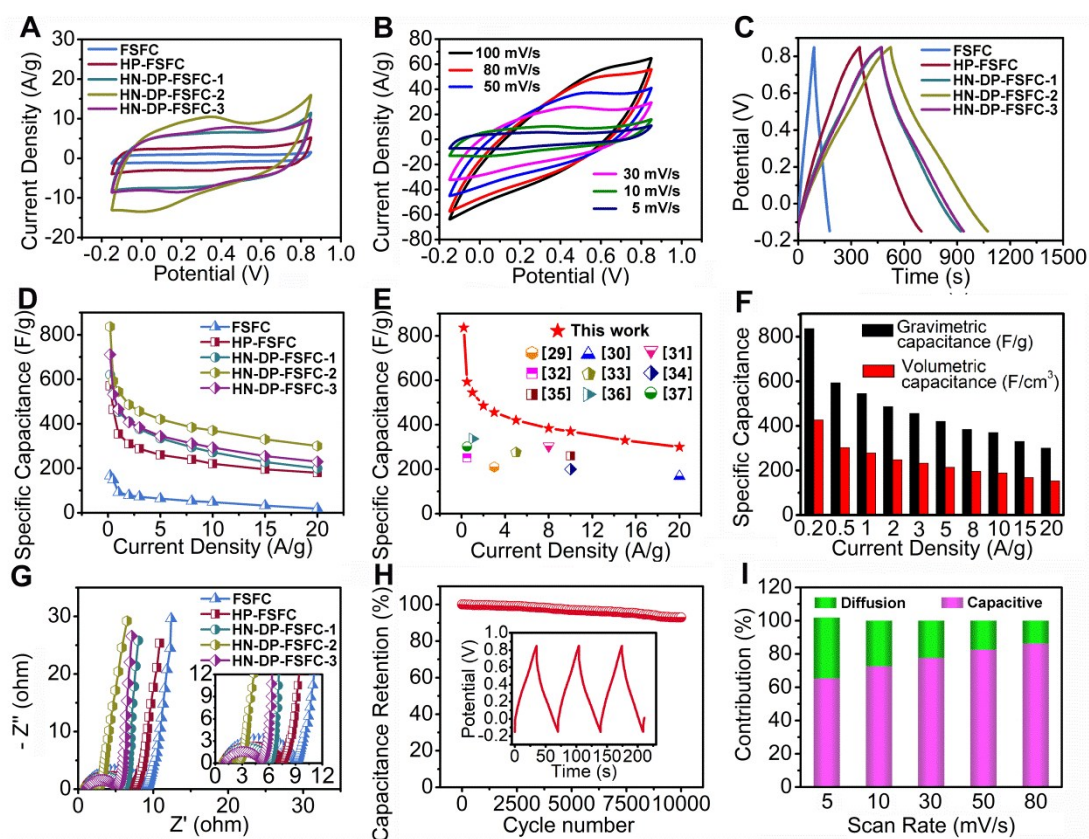


Fig. 3. Electrochemical performances of as-prepared samples in 2 M H₂SO₄ in the three electrode configuration: (A) CVs of all the samples at 10 mV/s; (B) CVs of HN-DP-FSFC-2 at different scan rates; (C) GCD curves at the current density of 1 A/g; (D) Specific capacitance at different current densities; (E) Comparison of specific capacitance with reported biochar materials; (F) Volumetric and gravimetric capacitances of ND-HP-FSFC-2 at different current densities; (G) Nyquist plots with the inset an enlargement of the high frequency region; (H) Cycling stability of ND-HP-FSFC-2 at 10 A/g after 10000 cycles with inset GCD curves; and (I) Normalized capacitive contribution percentages of HN-DP-FSFC-2 at different scan rates: surface controlled (magenta) and diffusion-controlled (green).

horizontal axis the equivalent series resistance (R_s).⁴¹ Among all the samples, HN-DP-FSFC-2 has the smallest values of both R_{ct} (1.54 Ω) and R_s (0.99 Ω) (Table S7), indicating its superior ion diffusion capability, and low charge transfer and internal resistances over the other samples. The corresponding Nyquist plot of the freeze-dried sample is also shown in Fig. S16. In addition, HN-DP-FSFC-2 also showed outstanding cycling stability, with capacitance retention of 93% even after 10,000 cycles at the high current density of 10 A/g (Fig. 3H). Corresponding GCD curves are included in the inset.

To further investigate the electrochemical behavior of the as-prepared samples, electrolytes with different pH values and ion dimensions, including Li₂SO₄, KOH, Na₂SO₄, and MgSO₄, were selected to test the performance of HN-DP-FSFC-2 in the three-electrode setup. The results are shown in Fig. S17. The current response in the CV curves is weakened with the capacitance at the current density of 0.2 A/g, which drops from 836 in H₂SO₄ to 504 (Li₂SO₄), 472 (KOH), 313 (Na₂SO₄), and 313 F/g (MgSO₄). The poor capacitive performance of HN-DP-FSFC-2 in KOH may be due to the lower molar conductivity of OH⁻ ions and lower ionic mobility, which is consistent with previous reports.^{42,43} Meanwhile, based on the comparison between H₂SO₄, Li₂SO₄, and Na₂SO₄, it can be observed that the larger electrolyte ions find it more difficult to

diffuse into the inner surfaces of the active materials, resulting in larger charge transfer resistance (Table S8), and thus the capacitive performance of HN-DP-FSFC-2 in Li₂SO₄ and Na₂SO₄ was weakened. Mg₂SO₄ with a smaller ion radius than Na₂SO₄ showed reduced capacitance at high current densities, which may be owing to the preferential electrosorption of hydrated Na⁺ rather than bivalent ions in the micropores.^{42,44} To investigate the influence of different nitrogen sources on the samples' electrochemical performance, the samples prepared from NH₄Cl and C₃H₆N₆ as the nitrogen dopants were also analyzed, and the detailed CV, GCD, and EIS results are presented in Fig. S18. The electrochemical performance was severely weakened in these cases, with the capacitance decreased to 311 and 292 at 0.2 A/g and R_{ct}/R_s increased to 3.26 Ω / 1.16 Ω and 5.86 Ω / 1.02 Ω , respectively, confirming that the dual-functional CON₂H₄ is an effective agent to enhance the electrochemical performance of carbonaceous materials.

To evaluate the detailed charge storage mechanism for surface-controlled (including both surface Faradaic reactions and ions adsorption/desorption) or diffusion-controlled processes, the CV curves of electrode materials at different scan rates were analyzed with b value vs. voltage plots, as shown in Fig. S19A. The detailed theoretical basis and methodology for evaluating the charge storage

mechanism can be found in the Supporting Information. The capacitive contribution of HN-DP-FSFC-2 calculated at different scan rates is listed in Fig. S19B and Fig. 3I. The surface capacitive contribution of HN-DP-FSFC-2 increased gradually with increasing scan rate from 65.31% at the scan rate of 5 mV/s to 72.59, 77.62, 82.54, and 86.27% at the scan rates of 10, 30, 50, and 80 mV/s, respectively.

The electrochemical performance of HN-DP-FSFC-2 was further investigated in symmetrical SCs device, and the results are shown in Fig. 4. In addition to H_2SO_4 , Li_2SO_4 , which was reported to efficiently block the corrosion of electrode materials and enable a higher working voltage for carbon based electrode by reducing capacity attenuation,⁴⁵ is also listed as the secondary aqueous electrolyte to evaluate the energy and power density of HN-DP-FSFC-2 in detail. The CV curve at the scan rate of 5 mV/s shows a typical quasi-rectangular shape in the potential window of 0 to 1.0 V in 2 M H_2SO_4 (Fig. 4A), while no obvious distortion is observed with increasing scan rate (Fig. S20A), confirming the great reversibility of HN-DP-FSFC-2 as a symmetric SC electrode.⁴⁶ Correspondingly, the operating voltage window of the active material in Li_2SO_4 was extended to 1.4 V, which is favorable for increasing its delivered energy density, considering that the energy density is proportional to the square of the permitted operating voltage window and the specific capacitance. The GCD profiles shown in Figs. 4B and 4C have some inflections, which are attributed to pseudocapacitive behavior from the heteroatoms introduced by the inherent elements in the raw material and the in-situ urea doping. The low current-resistance (IR) drops with the triangular GCD shapes demonstrate that the devices have excellent rate capability and low internal resistance.⁴⁷ The corresponding capacitance values of the cell (C_{cell}) were calculated based on the GCD curves, and the results are listed in Fig. 4D. The C_{cell} values are 169, 141, 109, 97.2, 91.2, 84, 76.8, and 74 F/g in 2 M H_2SO_4 at 0.2, 0.5, 1, 2, 3, 5, 8, and 10 A/g, respectively. Correspondingly, the C_{cell} values of a symmetric SC in 2 M Li_2SO_4 electrolyte showed a slight decrease to 134.2, 113.8, 84.1, 75.6, 69.2, 58.1, 46.7, and 43.3 F/g at 0.2, 0.5, 1, 2, 3, 5, 8, and 10 A/g respectively. The CV curve as the GCD profile of the samples with the loading mass increased to 5 mg/cm² is also shown in Fig. S20 (Figs. S20C and 20D). The lower capacitance of the symmetric devices compared with the three-electrode setup originates from the increased ion transfer resistance because of the separator in the cell and also the inefficient pseudocapacitance.⁴⁸

High energy density and excellent power density are viewed as important figures of merit to evaluate the practical applications of supercapacitors. The specific energy and power densities of HN-DP-FSFC-2 in aqueous electrolytes were compared with other reported biomass derived carbonaceous materials, and the Ragone plots are shown in Fig. 4E. The E_{cell} is 23.47, 19.58, 15.14, 13.50, 12.70, 11.67, 10.67, and 10.27 Wh/kg at 100, 250, 500, 1000, 1500, 2500, 4000, and 5000 W/kg, respectively, in 2 M H_2SO_4 . Due to the large operating voltage windows, the values of E_{cell} in 2 M Li_2SO_4 are further increased to 36.50, 30.80, 22.91, 20.57, 18.84, 15.82, 12.72, and 11.79 Wh/kg at 140, 350, 700, 1400, 2100, 3500, 5600, and 7000 W/kg, respectively. To the best of our knowledge, the excellent energy density of HN-DP-FSFC-2 achieved in Li_2SO_4 is the record value for any reported biomass-derived carbon in an aqueous

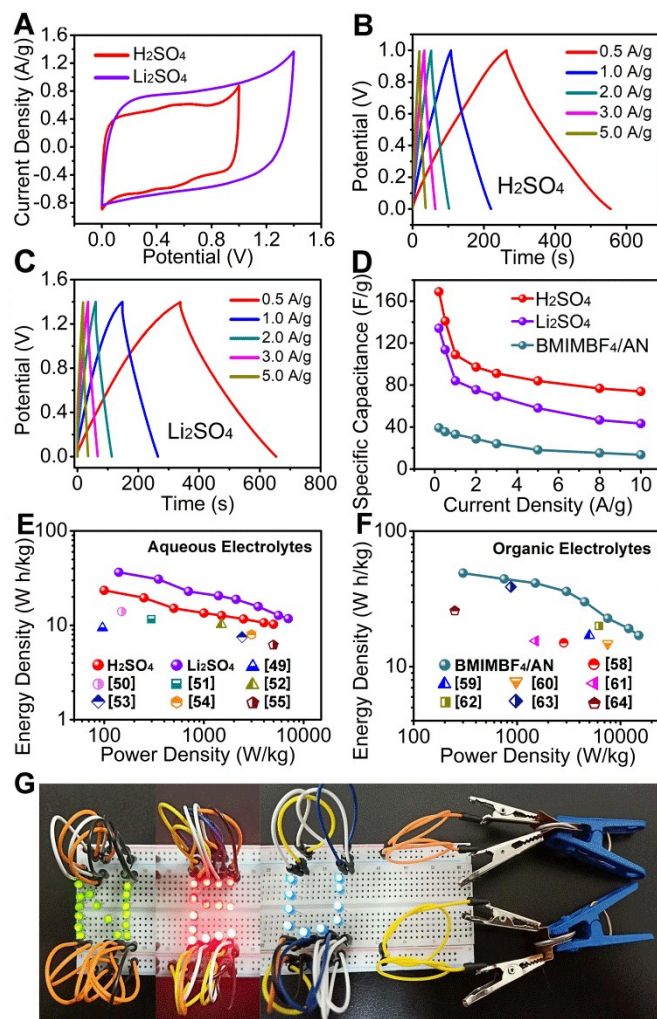


Fig. 4 Electrochemical performances of HN-DP-FSFC-2 in 2 M H_2SO_4 and 2 M Li_2SO_4 electrolytes in symmetrical SC cells: (A) CV curves at 5 mV/s; (B-C) GCD curves at different current densities; (D) C_{cell} as a function of current density; (E-F) Ragone plots of power density vs. energy density in different electrolytes. The scattered dots are the previously reported results on carbon based symmetric SCs; and (G) Coin cell used for lighting the “NEU” symbol.

electrolyte.^{18,49}

To enlarge the applied voltage operating window, BMIMBF₄/AN ionic liquid with high chemical and thermal stability as well as excellent conductivity⁵⁶ was used as the electrolyte for further investigating the energy storage performance of HN-DP-FSFC-2. See Fig. S20E and S20F for the CV and GCD curves. The symmetric supercapacitor device could be operated at the voltage of 3.0 V and scan rate of 100 mV/s without losing the rectangular-shaped curve. Based on the triangular GCD curves, we calculated the specific capacitance values as 39.2, 35.5, 33.1, 28.7, 24.1, 18.2, 15.3, and 13.6 F/g in BMIMBF₄/AN at 0.2, 0.5, 1, 2, 3, 5, 8, and 10 A/g, respectively (Fig. 4D). The decreased rate capability of the same material in the BMIMBF₄/AN electrolyte is attributed to the high viscosity of the electrolytes with larger effective ion diameters.⁵⁷ Owing to the high operating voltage window, the symmetric supercapacitor assembled from HN-DP-FSFC-2 could deliver a further high energy density of 49.00 Wh/kg at 300 W/kg. It could

still maintain 17.00 Wh/kg at 15000 W/kg (Ragone plots shown in Fig. 4F), which is far better than for comparable biomass carbonaceous materials in previous reports, making it one of the best biochars reported. The assembled supercapacitors for charging coin cells were also used to light small light emitting diode (LED) devices in the “NEU” symbol pattern (Fig. 4G), indicating their great potential for the applications in energy storage fields.

The high electrochemical performance of HN-DP-FSFC-2 may be attributed to the combined effects of its high SSA, suitable hierarchical porous structure with high microporosity, high electrical conductivity with small internal resistance, and abundant heteroatom dopants. Unlike previously reported activated carbonaceous materials with SSA smaller than 2000 m²/g,^{65,66} the SSA of HN-DP-FSFC-2 and HN-DP-FSFC-3 reached as high as 2351 and 2834 m²/g, respectively, close to the theoretical surface area of graphene (2630 m²/g).¹ A high SSA can offer abundant spaces for charge and ion accommodation, although an extremely high SSA also can lead to decreased electrochemical performance due to the decreased effective accessible area. A suitably interconnected pore structure is also important. Herein, the addition of CON₂H₄ leads to secondary activation from CO₂ and other released gases, which generate massive micropores and small mesopores 2–4 nm in size based on the activation of KOH. High microporosity is one of the key factors contributing to the high capacitive performance in the current case, in which the percentages of electrochemically accessible micropores with sizes larger than 0.7–0.8 nm are increased after CON₂H₄ addition. Herein, we do not want to convey the impression that higher microporosity will lead to better capacitive performances. Micropores alone in the pore structure will lead to long ion diffusion distances and high internal transport resistance, which can significantly weaken the electrochemical performances of carbonaceous materials.^{67, 68} In the current case, the 2–4 nm mesopores induced by the CON₂H₄ can serve as buffer diffusion channels for decreasing the ion-transfer distances.¹¹ In other words, the high percentage of micropores with sizes larger than 0.7 nm can provide enough spaces for trapping the ions and electrons to form Helmholtz layers, while the presence of mesopores 2–4 nm in size provides the shortest ion diffusion “highways” through the diffusion layer, as shown in Figure S21. Therefore, the high surface area with the appropriate hierarchical porous structure, including high microporosity, small mesopores (2–4 nm), and macropores/inherent tubular structure from FSF for effective mass transfer to the inner surfaces of the active materials, provides efficient ion diffusion/adsorption paths and thus leads to the high electrochemical performance. N doping from CON₂H₄ addition leads to improved electrode wettability, while the high N-5 and N-6 percentages (72.8% for HN-DP-FSFC-2) also increase the electrical conductivity of the as-prepared materials with small internal resistance ($R_{ct} = 0.99 \Omega$; $R_s = 1.54 \Omega$). All of the aforementioned microstructural and morphological features promote the high electrochemical performance of the as-prepared carbon.

Conclusions

In summary, an in-situ N-doped hierarchical porous carbon material with high microporosity was successfully synthesized by processing the biomass precursor FSF. Coupled with Co²⁺ as the catalyst for

balancing the degree of graphitization and pre-impregnated KOH as the molten medium for activation, CON₂H₄ was used as the micromolecular dual-functional template for achieving in-situ nitridation as well as the creation of micropores and small size mesopores (2–4 nm). Due to the benefits of its high SSA (> 2300 m²/g), its hierarchical porous structure with high microporosity ($S_{micro}/S_{total} = 86.81\%$), its high N-5 and N-6 percentages from N-heteroatom doping (72.8%), and its excellent wettability ($\theta = 26.2^\circ$) and small internal resistance ($R_{ct} = 0.99 \Omega$; $R_s = 1.54 \Omega$), the as-prepared HN-DP-FSFC-2 showed a record high specific capacitance for a biomass derived carbonaceous material of 836.4 F/g in 2 M H₂SO₄ at 0.2 A/g in a three-electrode system. Its volumetric capacitance also reached as high as 426.6 F/cm³. This electrode material also showed outstanding cycling stability, with capacitance retention of 92.96% after 10,000 cycles at 10 A/g. We also studied different control samples to investigate the influence of the pore structure and heteroatom engineering on the electrochemical performance. These control samples include the ones with different CON₂H₄ contents, FSFC (without the addition of KOH and CON₂H₄), HP-FSFC (without the addition of CON₂H₄), an ice-templated sample for introducing more macropores, and nitrogen-doped samples with NH₄Cl and C₃H₆N₆. Different electrolytes, such as KOH, Li₂SO₄, Na₂SO₄, and MgSO₄, were also used to optimize the selection of electrolytes. The assembled symmetrical SCs exhibited high-level energy density of 36.50 Wh/Kg at the power density of 140 W/kg in 2 M Li₂SO₄, which is the record energy density value for biomass-derived carbon in aqueous electrolytes. The energy density can be further increased to 49.00 Wh/kg in 1 M BMIMBF₄/AN ionic liquid. The present work proposes a facile synthesis approach to treating renewable biomass derivatives to fabricate advanced carbonaceous materials for high performance supercapacitor electrodes, and its applications can probably be extended to other energy storage devices, including Li/Na ion batteries, electrocatalysts, Li-S batteries, etc.

Conflicts of interest

There are no conflicts to declare.

Acknowledgements

C. Chang and M. Li contributed equally to this work. This work is supported by the National Nature Science Foundation of China (51574062), the Fundamental Research Funds for the Central Universities (N182505036) and LiaoNing Revitalization Talents Program (XLYC1807123). We also want to appreciate Dr Tania Silver for critical reading about this work.

Notes and references

- 1 T. Lin, I.-W. Chen, F. Liu, C. Yang, H. Bi, F. Xu and F. Huang, *Science*, 2015, **350**, 1508–1513.
- 2 K. Shi, X. Yang, E. D. Cranston and I. Zhitomirsky, *Adv. Funct. Mater.*, 2016, **26**, 6437–6445.
- 3 K. Shi, M. Ren and I. Zhitomirsky, *ACS Sustain. Chem. Eng.*, 2014, **2**, 1289–1298.
- 4 D. Sheberla, J. C. Bachman, J. S. Elias, C.-J. Sun, Y. Shao-Horn and M. Dincă, *Nat. Mater.*, 2016, **16**, 220–224.

- 5 Y. Zhang, X. Liu, S. Wang, L. Li and S. Dou, *Adv. Energy Mater.*, 2017, **7**, 1700592–1700614.
- 6 L.-F. Chen, Y. Lu, L. Yu and X. W. Lou, *Energ. Environ. Sci.*, 2017, **10**, 1777–1783.
- 7 X. Wang, Y. Zhang, C. Zhi, X. Wang, D. Tang, Y. Xu, Q. Weng, X. Jiang, M. Mitome, D. Golberg and Y. Bando, *Nat. Commun.*, 2013, **4**, 2905–2912.
- 8 Y. Zhao, M. Liu, X. Deng, L. Miao, P. K. Tripathi, X. Ma, D. Zhu, Z. Xu, Z. Hao and L. Gan, *Electrochim. Acta*, 2015, **153**, 448–455.
- 9 J. Li, N. Wang, J. Tian, W. Qian and W. Chu, *Adv. Funct. Mater.*, 2018, **28**, 1806153–1806161.
- 10 K. Shi and I. Zhitomirsky, *Electrochim. Acta*, 2015, **174**, 588–595.
- 11 C. Long, X. Chen, L. Jiang, L. Zhi and Z. Fan, *Nano Energy*, 2015, **12**, 141–151.
- 12 L. Jiang, J. Yan, L. Hao, R. Xue, G. Sun, and B. Yi, *Carbon*, 2013, **56**, 146–154.
- 13 Z. Li, L. Zhang, B. S. Amirkhiz, X. Tan, Z. Xu, H. Wang, B. C. Olsen, C. M. B. Holt and D. Mitlin, *Adv. Energy Mater.*, 2012, **2**, 431–437.
- 14 M. Klotz, I. Amirouche, C. Guizard, C. Viazzi and S. Deville, *Adv. Eng. Mater.*, 2012, **14**, 1123–1127.
- 15 Y. An, Z. Li, Y. Yang, B. Guo, Z. Zhang, H. Wu and Z. Hu, *Adv. Mater. Interfaces*, 2017, **4**, 1700033–1700042.
- 16 H. Wang, X. Liu, S. Wang, and L. Li, *Appl. Catal. B-Environ.*, 2018, **222**, 209–218.
- 17 Z. Mou, X. Chen, Y. Du, X. Wang, P. Yang and S. Wang, *Appl. Surf. Sci.*, 2011, **258**, 1704–1710.
- 18 Y. Zhang, X. Liu, S. Wang, S. Dou and L. Li, *J. Mater. Chem. A*, 2016, **4**, 10869–10877.
- 19 M. A. Yahya, Z. Al-Qodah and C. W. Z. Ngah, *Renew. Sust. Energ. Rev.*, 2015, **46**, 218–235.
- 20 X. Wang, X. Li, L. Zhang, Y. Yoon, P. K. Weber, H. Wang, J. Guo and H. Dai, *Science*, 2009, **324**, 768–771.
- 21 Y. Shao, J. Li, Y. Li, H. Wang, Q. Zhang and R. B. Kaner, *Mater. Horiz.*, 2017, **4**, 1145–1150.
- 22 D. Hulicova-Jurcakova, M. Seredych, G. Q. Lu and T. J. Bando, *Adv. Funct. Mater.*, 2010, **19**, 438–447.
- 23 B. Li, R. Shi, C. Han, H. Li, L. Xu, T. Zhang, J. Li, Z. Lin, C. Wong and F. Kang, *J. Mater. Chem. A*, 2018, **6**, 17057–17066.
- 24 F. Su, C. K. Poh, J. S. Chen, G. Xu, D. Wang, Q. Li, J. Lin and X. W. Lou, *Energy Environ. Sci.*, 2011, **4**, 717–724.
- 25 Y. Zhang, Q. Ma, S. Wang, X. Liu, and L. Li, *ACS Nano*, 2018, **12**, 4824–4834.
- 26 Y. Yao, Y. Zhang, L. Li, S. Wang, S. Dou and X. Liu, *ACS Appl. Mater. Inter.*, 2017, **9**, 34944–34953.
- 27 J. Yang, X. Zhou, D. Wu, X. Zhao and Z. Zhou, *Adv. Mater.*, 2016, **29**, 1604108–1604112.
- 28 S. Yang, S. Wang, X. Liu and L. Li, *Carbon*, 2019, **147**, 540–549.
- 29 M. Liu, J. Niu, Z. Zhang, M. Dou and F. Wang, *Nano Energy*, 2018, **51**, 366–372.
- 30 J.-H. Choi, C. Lee, S. Cho, G. D. Moon, B. kim, H. Chang and H. D. Jang, *Carbon*, 2018, **132**, 16–24.
- 31 B. Zhu, B. Liu, C. Qu, H. Zhang, W. Guo, Z. Liang, F. Chen and R. Zou, *J. Mater. Chem. A*, 2018, **6**, 1523–1530.
- 32 S. Gao, X. Li, L. Li and X. Wei, *Nano Energy*, 2017, **33**, 334–342.
- 33 S.-Y. Lu, M. Jin, Y. Zhang, Y.-B. Niu, J.-C. Gao and C. M. Li, *Adv. Energy Mater.*, 2017, **8**, 1702545–1702553.
- 34 W.-L. Song, X. Li and L.-Z. Fan, *Energy Storage Mater.*, 2016, **3**, 113–122.
- 35 Q. Wang, B. Qin, X. Zhang, X. Xie, L. Jin and Q. Cao, *J. Mater. Chem. A*, 2018, **6**, 19653–19663.
- 36 S. Liu, Y. Zhao, B. Zhang, H. Xia, J. Zhou, W. Xie and H. Li, *J. Power Sources*, 2018, **381**, 116–126.
- 37 X. Hao, J. Wang, B. Ding, Y. Wang, Z. Chang, H. Dou and X. Zhang, *J. Power Sources*, 2017, **352**, 34–41.
- 38 B. Liu, Y. Liu, H. Chen, M. Yang and H. Li, *J. Power Sources*, 2017, **341**, 309–317.
- 39 J. Pang, W. Zhang, J. Zhang, G. Cao, M. Han and Y. Yang, *Green Chem.*, 2017, **19**, 3916–3926.
- 40 L. Yan, D. Li, T. Yan, G. Chen, L. Shi, Z. An and D. Zhang, *ACS Sustain. Chem. Eng.*, 2018, **6**, 5265–5272.
- 41 Y. Sun, R. B. Sills, X. Hu, Z. W. Seh, X. Xiao, H. Xu, W. Luo, H. Jin, Y. Xin, T. Li, Z. Zhang, J. Zhou, W. Cai, Y. Huang and Y. Cui, *Nano Lett.*, 2015, **15**, 3899–3906.
- 42 E. Avraham, B. Yaniv, A. Soffer and D. Aurbach, *J. Phys. Chem. C*, 2008, **112**, 7385–7389.
- 43 X. Zhang, X. Wang, L. Jiang, H. Wu, C. Wu and J. Su, *J. Power Sources*, 2012, **216**, 290–296.
- 44 F. Béguin, V. Presser, A. Balducci and E. Frackowiak, *Adv. Mater.*, 2014, **26**, 2219–2251.
- 45 Y. Zhang, S. Yang, S. Wang, X. Liu and L. Li, *Energy Storage Mater.*, 2019, **18**, 447–455.
- 46 Y. Wang, X. C. Wang and M. Antonietti, *Angew. Chem. Int. Ed.*, 2012, **51**, 68–89.
- 47 X. Xia, D. Chao, C. F. Ng, J. Lin, Z. Fan, H. Zhang, Z. Shen and H. J. Fan, *Mater. Horiz.*, 2014, **2**, 237–244.
- 48 S. Yang, Y. Zhang, S. Wang, J. Shi, X. Liu and L. Li, *J. Mater. Chem. A*, 2019, DOI: 10.1039/C9TA04516C.
- 49 Q. Liang, L. Ye, Z.-H. Huang, Q. Xu, Y. Bai, F. Kang and Q.-H. Yang, *Nanoscale*, 2014, **6**, 13831–13837.
- 50 P. Yang, J. Xie and C. Zhong, *ACS Appl. Energy Mater.*, 2018, **1**, 616–622.
- 51 Z. Xu, Y. Li, D. Li, D. Wang, J. Zhao, Z. Wang, M. N. Banis, Y. Hu and H. Zhang, *Appl. Surf. Sci.*, 2018, **444**, 661–671.
- 52 X. Kang, H. Zhu, C. Wang, K. Sun and J. Yin, *J. Colloid Interf. Sci.*, 509 (2018), **509**, 369–383.
- 53 X. Han, H. Jiang, Y. Zhou, W. Hong, Y. Zhou, P. Gao, R. Ding and E. Liu, *J. Alloy. Compd.*, 744 (2018), **744** 544–551.
- 54 W.-J. Liu, K. Tian, Y.-R. He, H. Jiang and H.-Q. Yu, *Environ. Sci. Technol.*, 2014, **48**, 13951–13959.
- 55 W. Hong, L. Wang, K. Liu, X. Han, Y. Zhou, P. Gao, R. Ding and E. Liu, *J. Alloy. Compd.*, 2018, **746**, 292–300.
- 56 W. Liu, X. Yan, J. Lang, J. Pu and Q. Xue, *New J. Chem.*, 2013, **37**, 2186–2195.
- 57 L. Zhang and X. Zhao, *Chem. Soc. Rev.*, 2009, **38** 2520–2531.
- 58 W. Qu, Y. Xu, A. Lu, X. Zhang and W. Li, *Bioresource Technol.*, 2015, **189**, 285–291.
- 59 G. A. Ferrero, A. B. Fuertes and M. Sevilla, *J. Mater. Chem. A*, 2015, **3**, 2914–2923.
- 60 J. Zhou, X. Yuan, W. Xing, W. Si and S. Zhuo, *Carbon*, 2010, **48**, 2765–2772.
- 61 Y. J. Kang, S.-J. Chun, S.-S. Lee, B.-Y. Kim, J. H. Kim, H. Chung, S.-Y. Lee and W. Kim, *ACS Nano*, 2012, **6**, 6400–6406.
- 62 M. Kota, M. Jana and H. S. Park, *J. Power Sources*, 2018, **399**, 83–88.
- 63 T. Kesavan, T. Partheeban, M. Vivekanantha, M. Kundu, G. Maduraiveeran and M. Sasidharan, *Micropor. Mesopor. Mat.*, 2019, **274**, 236–244.
- 64 Y. Zhong, T. Shi, Y. Huang, S. Cheng, G. Liao and Z. Tang, *Electrochim. Acta*, 2018, **269**, 676–685.
- 65 C. Chang, H. Wang, Y. Zhang, S. Wang, X. Liu, and L. Li, *ACS Sustainable Chem. Eng.*, 2019, **7**, 10763–10772.
- 66 J. Wei, D. Zhou, Z. Sun, Y. Deng, Y. Xia and D. Zhao, *Adv. Funct. Mater.*, 2012, **23**, 2322–2328.
- 67 J. Niu, R. Shao, J. Liang, M. Dou, Z. Li, Y. Huang and F. Wang, *Nano Energy*, 2017, **36**, 322–330.
- 68 T. Xu, S. Wang, L. Li and X. Liu, *Appl. Catal. A-Gen.*, 2019, **575**, 132–141.